

Measurement-Based Wide-Area Damping of Inter-Area Oscillations based on MIMO Identification

Abilash Thakallapelli¹, Sukumar Kamalasan^{1*}

¹ Electrical and Computer Engineering, UNC Charlotte, Charlotte, USA

* E-mail: skamalas@uncc.edu

Abstract:

Interconnected power grid exhibits oscillatory response after a disturbance in the system. One such type of oscillations, the inter-area oscillations has the oscillation frequency in the range of 0.1 to 1 Hz. The damping of inter-area oscillations is difficult with local controllers, but it can be achieved using a Wide Area Damping Controller (WADC). For effective control, the input to the WADC should be the most observable signal and the WADC output should be sent to the most controllable generator. This paper presents a measurement-based novel algorithm for multi-input-multi-output (MIMO) transfer function identification of the power system based on optimization to estimate such oscillation frequencies. Based on the MIMO transfer function the optimal control loop for WADC is estimated. The WADC design is based on the discrete linear quadratic regulator (DLQR) and Kalman filtering for damping of inter-area oscillations. Since the MIMO identification is based on actual measurements, the proposed method can accurately monitor changes in the power grid whereas the conventional methods are based on small-signal analysis of a linearized model which does not consider changing operating conditions. The overall algorithm is implemented and validated on a RTDS/RSCAD[®] and MATLAB[®] real-time co-simulation platform using two-area and IEEE 39 bus power system models.

1 Introduction

The increase in penetration of renewable energy sources and deregulation made the power system to operate near its rated operating limits. Under these circumstances, if there is a disturbance in the system this could affect the power system reliability and security. The oscillatory response which arise due to such disturbances have to be damped effectively and these oscillations are of two types 1) Local oscillations, and 2) Inter-area oscillations. The local oscillations have frequencies greater than 1 Hz and inter-area oscillations frequency lies in the range of 0.1 to 1 Hz [1]. During inter-area oscillations generators in one coherent area swing together against other area generators [2]. In general, such oscillations are suppressed using supplementary control techniques like power system stabilizers (PSS) [3], flexible alternating current transmission systems (FACTS) devices [4] and high-voltage direct current (HVDC) links [5]. However, such controllers are effective only during local oscillations. As the inter-area oscillations may destabilize the power system [6] it should be damped effectively.

In literature, several methodologies are presented to damp inter-area oscillations using a wide area control loop which is effective to damp an inter-area mode of interest. The wide area control loop is based on the most observable control signal which is input to the wide-area controller and the output of the controller is sent to the most controllable generator. This input/output combination can be estimated based on residue analysis [7–9], combination of residue and relative gain array (RGA) method [10], and a joint observability-controllability measure [11, 12]. In all these methods, the control-loop selection is based on linearizing the system at an operating point and analyzing the state space matrices obtained thereafter. If the system operating point changes then the control-loop obtained at a different operating point may not be valid and a new control-loop is to be estimated based on current operating point. However, linearizing the complex power system model every time as the operating point changes are tedious and an accurate model of the power system for the current operating point may not be always readily available.

To overcome the drawbacks of linearization based methods, measurement based methods are adapted. In such methods, using the

measurements, the MIMO model of the power system can be estimated directly without the need for having a detailed model of the power system. Since the changing dynamics/operating points of the system are captured in the measurement data, the MIMO model thus obtained can be used for mode and control loop estimation. The measurement-based methodologies gained interest with the advent of phasor measurement unit (PMUs), and modern communication infrastructure. A mode estimation method based on prony analysis is discussed in [13], however the mutual coupling between different MIMO loops is not considered in the mode estimation. In [14], a measurement based method is discussed which is based on using simplified power system model and wide-area measurement system (WAMS) data. However the problems related to the selection of optimal control loop is not addressed here. The use of PMU data for wide-area control of STATCOM is addressed in [15], but the effect of mutual coupling during mode estimation and optimal signal selection is not represented. A power system model using MIMO identification based on auto-regressive moving average exogenous (ARMAX) methodology is developed in [16] but an optimal method for signal selection is not addressed.

To address some of the existing issues, in this paper, a novel measurement based MIMO system identification technique for wide-area control considering mutual coupling between different control loops is presented. The identified MIMO system is used for 1) inter-area oscillation frequency estimation, 2) optimal control loop estimation, and 3) design of wide area controller. To summarize, the major contributions of this work are:

- A measurement based MIMO framework considering the mutual coupling of loops for mode estimation.
- A method for online optimal control loop selection for WADC using residue analysis based on measurement data.
- An online WADC based on DLQR and KF techniques which uses the extracted state space matrices from identified MIMO system.
- A real-time co-simulation test bed for measurement based MIMO and WADC considering mutual coupling between different control loops.

The rest of the paper is organized as follows: Section II discusses the overall architecture and power system division based on

coherency is discussed. In section III, measurement based MIMO identification is discussed and section IV discusses real-time implementation of MIMO identification. Section V discusses optimal wide area control loop selection and Section VI discusses measurement based DLQR and Kalman filter design. Section VII discusses simulation results and Section VIII concludes the paper.

2 Dividing Power System Based on Coherency and Overall Architecture

Design of the proposed architecture is based on dividing the power system into areas using coherency grouping and inter tie-line connections between areas. First, the active power flow deviation ($\Delta P = P_{rated} - P_{actual}$) through the tie-lines are used as input signal to the WADC [17]. Then MIMO identification is designed to estimate an optimal control loop to damp the inter-area mode oscillation. Finally, WADC is designed with a measurement based discrete linear quadratic regulator (DLQR) integrated in kalman filtering (KF) technique. Fig. 1 shows the flowchart of the proposed methodology. The efficacy of the proposed algorithm is verified by implementing on a RTDS/RSCAD and MATLAB real-time test bed using two-area and IEEE 39 bus power system models.

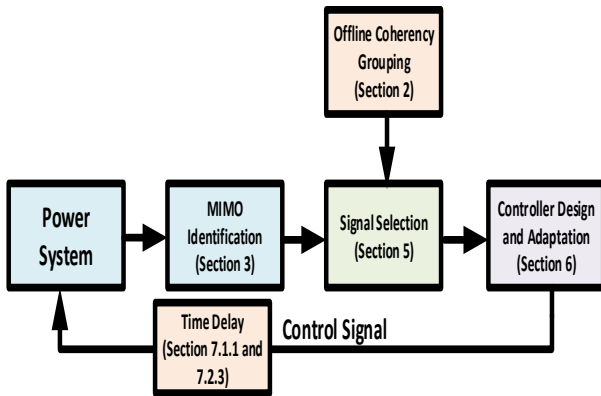


Fig. 1: Flow-chart of the proposed methodology

For grouping of power grid, slow coherency grouping method is considered. Please refer [18] for further details of slow coherency grouping method. This algorithm is implemented on two-area power system (Fig. 2) as well as IEEE 39 bus (Fig. 7) power system models. Further, tie-line power flow information is used in deciding the wide-area control action.

2.1 Coherency grouping of two-area system model

On applying the slow coherency grouping method to the two-area power system model, it is found that generators 1 and 2 are in one area and the remaining generators are in other area. To validate this grouping from the actual response of the system a 3-ph fault is created at 4s for a duration of 0.05s on bus-8 and generators inter-area dynamics are observed. Fig. 3 shows the speed deviation of generators from its rated speed (i.e $2\pi f$, where f is fundamental frequency in Hz). It can be seen that generators 1,2 swing against generators 3 and 4. Based on this grouping the test model is divided into two areas (groups) as shown in Fig. 2 and Table 1. From Fig. 2 it can be seen that lines connecting Bus-7 to Bus-8 to Bus-9, and Bus-7 to Bus-9 are the two tie-lines. The active power flow deviation of these two lines are represented as ΔP_1 and ΔP_2 respectively.

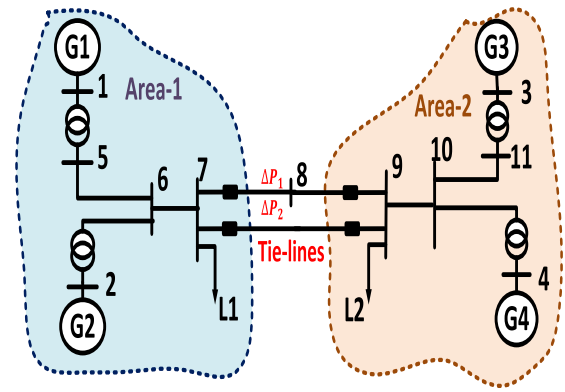


Fig. 2: Two-area power system model

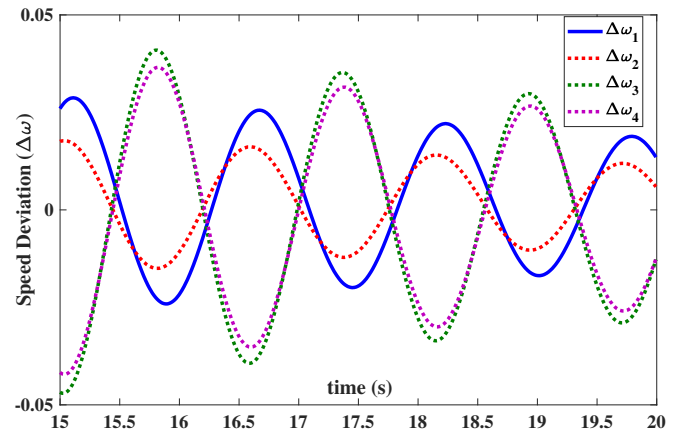


Fig. 3: Speed deviation (rad/s) (two-area system)

2.2 Coherency grouping of IEEE 39 bus system

The IEEE 39 bus system (Fig. 4) coherent groups of generators are obtained using the slow coherency grouping algorithm as shown in Table 1. For validation purpose, a 3-ph fault is created on Bus-14 at 4s for a duration of 0.1s. Fig. 5, Fig. 6, and Fig. 7 shows the speed deviations of generators in groups-1, 2, and 3 respectively. From Fig. 4 it can be seen that lines connecting Bus-39 to Bus-1, Bus-39 to Bus-9, Bus-3 to Bus-4, Bus-14 to Bus-15, and Bus-16 to Bus-17 are the tie-lines. The active power flow deviation of these tie-lines are represented as ΔP_1 , ΔP_2 , ΔP_3 , ΔP_4 , and ΔP_5 respectively.

3 Measurement based MIMO Identification

Most of the physical world systems are MIMO and traditionally the dynamics of these system are analyzed using linearized model at an operating point and estimating modes and mode shapes from the state space matrices thus obtained after linearization. However, linearizing a complex system requires accurate model which represents the current operating point of the system, This is often difficult to build. A measurement based MIMO identification can overcome

Table 1 Coherency grouping of power system models

Test System	Slow Coherency
Two Area	Group-1: 1,2 Group-2: 3,4
IEEE 39-BUS	Group-1: 4,5,6,7 Group-2: 1,8,9 Group-3: 2,3 Group-4: 10

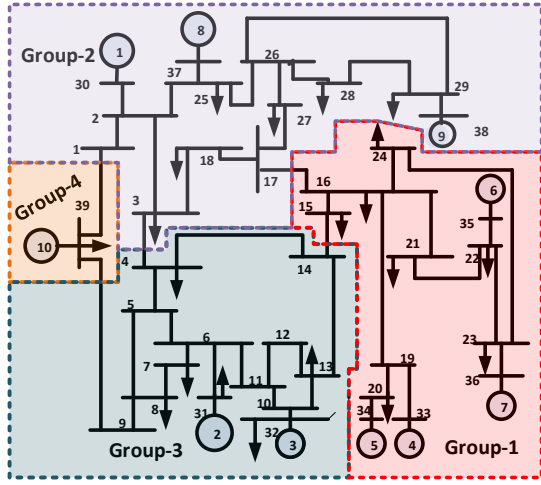


Fig. 4: 39-bus power system model

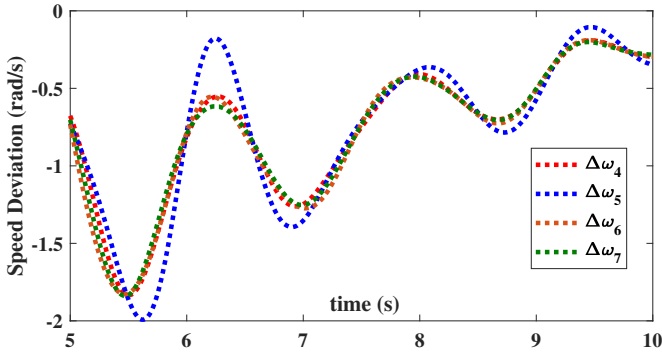


Fig. 5: Speed Deviation (Group-1)

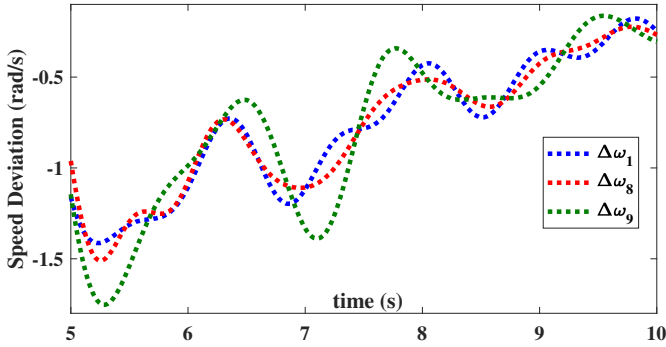


Fig. 6: Speed Deviation (Group-2)

modeling accuracy if identified using measured data. However, the coupling effects between different input/output combinations should be considered while developing an MIMO model. The methodology is discussed using an example in Subsection 3.1.

3.1 MIMO transfer function from state space matrices

Consider a system with two inputs, u_1 and u_2 , and two outputs, y_1 and y_2 represented by differential equation [19] as follows:

$$y_1'' + a_1 y_1' + a_0(y_1 + y_2) = u_1(t) \quad (1)$$

$$y_2' + a_2(y_2 - y_1) = u_2(t) \quad (2)$$

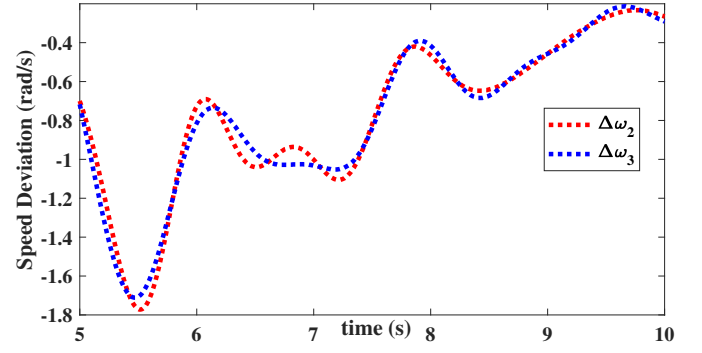


Fig. 7: Speed Deviation (Group-3)

where superscripts y' and y'' indicates first and second order differential equations respectively. In state-space form (1) and (2) gives:

$$x_1 = y_1 \quad (3)$$

$$x_4 = y_2 = x_3 \quad (4)$$

$$x_1' = y_1' = x_2 \quad (5)$$

$$x_2' = -a_1 x_2 - a_0(x_1 + x_4) + u_1(t) \quad (6)$$

$$x_4' = -a_2(x_4 - x_1) + u_2(t) \quad (7)$$

Now rearranging (3) to (7) to get state space equations.

$$x' = \underbrace{\begin{bmatrix} 0 & 1 & 0 & 0 \\ -a_0 & -a_1 & 0 & -a_0 \\ 0 & 0 & 0 & 1 \\ a_2 & 0 & 0 & -a_2 \end{bmatrix}}_A x + \underbrace{\begin{bmatrix} 0 & 0 \\ 1 & 0 \\ 0 & 0 \\ 0 & 1 \end{bmatrix}}_B \begin{bmatrix} u_1 \\ u_2 \end{bmatrix} \quad (8)$$

$$\begin{bmatrix} y_1 \\ y_2 \end{bmatrix} = \underbrace{\begin{bmatrix} 1 & 0 & 0 & 0 \\ 0 & 0 & 0 & 1 \end{bmatrix}}_C x \quad (9)$$

Converting (8) and (9) into transfer function form

$$G(s) = C(s\mathbf{I} - \mathbf{A})^{-1}\mathbf{B} = \begin{bmatrix} G_{11}(s) & G_{12}(s) \\ G_{21}(s) & G_{22}(s) \end{bmatrix} \quad (10)$$

where \mathbf{I} is the identity matrix and

$$G_{11}(s) = \frac{s + a_2}{s^3 + (a_1 + a_2)s^2 + (a_0 + a_1a_2)s + 2a_0a_2}$$

$$G_{12}(s) = \frac{-a_0}{s^3 + (a_1 + a_2)s^2 + (a_0 + a_1a_2)s + 2a_0a_2}$$

$$G_{21}(s) = \frac{a_2}{s^3 + (a_1 + a_2)s^2 + (a_0 + a_1a_2)s + 2a_0a_2}$$

$$G_{22}(s) = \frac{s^2 + a_1s + a_0}{s^3 + (a_1 + a_2)s^2 + (a_0 + a_1a_2)s + 2a_0a_2}$$

Equation (10) can be represented in discrete time domain by replacing s with $\frac{2(1-z^{-1})}{T_s(1+z^{-1})}$ (tustin approximation), where T_s is the sampling time.

$$G(z^{-1}) = \begin{bmatrix} G_{11}(z^{-1}) & G_{12}(z^{-1}) \\ G_{21}(z^{-1}) & G_{22}(z^{-1}) \end{bmatrix} \quad (11)$$

The objective here is to identify the MIMO transfer function as shown in (10) and (11) using the measurement data without having

any knowledge of the physical system model. If MIMO identification is based on different input/output combinations separately, mutual coupling between loops are ignored. However, if we observe the individual transfer function of (10), it can be seen that all the transfer functions have same denominator coefficients (i.e eigen values of the system) while numerator coefficients differ. This ensures mutual coupling between loops in MIMO system. So our objective is to formulate a MIMO identification using input/output measurement with same denominator coefficients but different numerator coefficients.

3.2 Measurement based MIMO identification considering mutual coupling

For measurement based MIMO identification the input data u_p is the voltage reference to the exciter of the synchronous machine and the output is the tie-line active power deviation, ΔP_m . The input/output measurement channel is as illustrated in Fig. 8. The real-life system and EMT based real-time simulator is in discrete-domain, so the MIMO formulation of the power system is also modeled in discrete time domain with p inputs and m outputs as represented in (12). The individual transfer function corresponding to each input/output loop is estimated using the proposed methodology for MIMO identification considering the mutual coupling between different loops. This can be written as

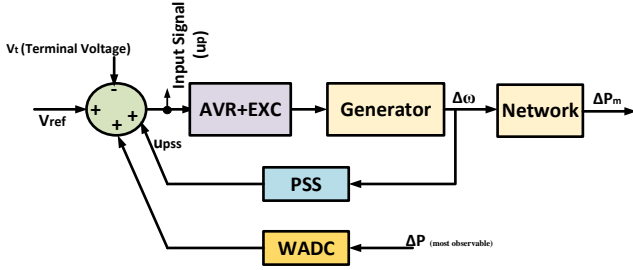


Fig. 8: Input and output measurements

$$\Delta P(z^{-1}) = G(z^{-1})U(z^{-1}) \quad (12)$$

where

$$\Delta P(z^{-1}) = \begin{bmatrix} \Delta P_1(z^{-1}) \\ \vdots \\ \Delta P_m(z^{-1}) \end{bmatrix}, U(z^{-1}) = \begin{bmatrix} u_1(z^{-1}) \\ \vdots \\ u_p(z^{-1}) \end{bmatrix}$$

$$G(z^{-1}) = \begin{bmatrix} G_{11}(z^{-1}) & \dots & G_{1p}(z^{-1}) \\ \vdots & \ddots & \vdots \\ G_{m1}(z^{-1}) & \dots & G_{mp}(z^{-1}) \end{bmatrix}$$

and

$$G_{mp}(z^{-1}) = \frac{\Delta P_m(z^{-1})}{u_p(z^{-1})} \quad (13)$$

$$= \frac{b_0^h + b_1^h z^{-1} + \dots + b_k^h z^{-k}}{1 + a_1 z^{-1} + a_2 z^{-2} + \dots + a_k z^{-k}}$$

where u_p and ΔP_m are the input and output signal data, h is the element number in matrix, and k is the order of transfer function. It can be seen from (13) that for all transfer functions the denominator coefficients are same but numerator coefficients differ. This ensures that mutual coupling effect is taken into account. The steps for MIMO transfer function identification is as follows:

3.2.1 *Step-1:* The equation (12) is rewritten for N observation window length as shown in (14).

$$X_{His}^h = X_{Num}^h \begin{bmatrix} b_0^h \\ \vdots \\ b_k^h \end{bmatrix} + X_{Den}^h \begin{bmatrix} a_1 \\ \vdots \\ a_k \end{bmatrix} \quad (14)$$

where

$$X_{His}^h = \begin{bmatrix} \Delta P_1(z^{-1}) \\ \vdots \\ \Delta P_m(z^{-1}) \end{bmatrix}$$

$$X_{Num}^h = \begin{bmatrix} u_p(z-1) & \dots & u_p(z-k) \\ \vdots & \ddots & \vdots \\ u_p(z-N) & \dots & u_p(z-N+1-k) \end{bmatrix}$$

$$X_{Den}^h = \begin{bmatrix} \Delta P_m(z-1) & \dots & \Delta P_m(z-k) \\ \vdots & \ddots & \vdots \\ \Delta P_m(z-N) & \dots & \Delta P_m(z-N+1-k) \end{bmatrix}$$

3.2.2 *Step-2:* For all input/output loops, concatenate X_{His}^h and is represented as (15)

$$\underbrace{\begin{bmatrix} X_{His}^1 \\ X_{His}^2 \\ \vdots \\ X_{His}^h \end{bmatrix}}_{X_H} = \underbrace{\begin{bmatrix} X_{Num}^1 \\ X_{Num}^2 \\ \vdots \\ X_{Num}^h \end{bmatrix}}_{X_N} \begin{bmatrix} b_0^1 \\ \vdots \\ b_k^1 \\ b_0^2 \\ \vdots \\ b_k^2 \\ \vdots \\ b_0^h \\ \vdots \\ b_k^h \end{bmatrix} + \underbrace{\begin{bmatrix} X_{Den}^1 \\ X_{Den}^2 \\ \vdots \\ X_{Den}^h \end{bmatrix}}_{X_D} \begin{bmatrix} a_1 \\ \vdots \\ a_k \end{bmatrix} \quad (15)$$

3.2.3 *Step-3:* The numerator and denominator coefficients are estimated using an optimization algorithm where the optimization function is represented as (16)

$$\text{minimize } \|X_H - [X_N + X_D]\| \quad (16)$$

Initial conditions for the numerator ($b_0^h, b_1^h, \dots, b_k^h$) and denominator (a_1, a_2, \dots, a_k) coefficients are estimated from a least squares technique formulated as constrained nonlinear multivariable function. For this the MATLAB based *fmincon* function is used to solve the unknowns.

4 Real-time implementation of MIMO identification

The proposed MIMO identification of the power system is implemented on a RTDS/RSCAD and MATLAB co-simulation test bed as shown in Fig. 9. The power system is modeled in RTDS/RSCAD and the MIMO identification algorithm is implemented in MATLAB. The real-time measured data from the digital simulator is processed through an Ethernet based socket connection [20]. The data received

is then processed for MIMO identification. Also the identified transfer function is used to estimate an optimal control loop. The control signal is then send back to the power system model in the digital simulator. Since this approach is implemented using RTDS, the process exactly emulates the real-life scenario. Thus the designed controller can be tested using this co-simulation platform before implementing in field.

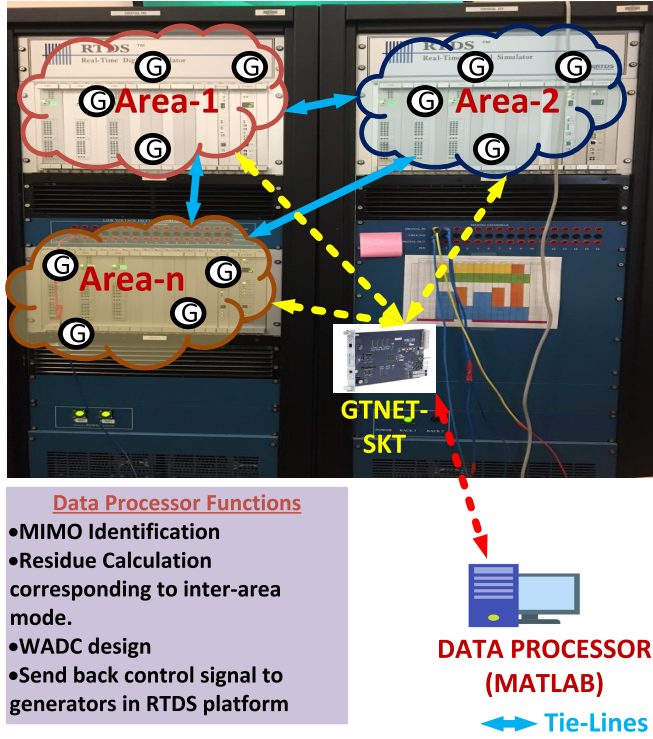


Fig. 9: Real-time experimental setup

4.1 Data Criteria

The proposed algorithm is first validated on the two-area power system model (Fig. 2). The measurement data u_p and ΔP_m of all generators are extracted with a sampling time (T_s) of 0.0032s. The data-set is then down-sampled by a factor 10 so that the new sampling time will be 0.032s. The new sampling time after down-sampling is used to estimate inter-area modes. The inter-area frequency range is between 0.1 to 1Hz so for a successful estimation of inter-area frequency a window length of two cycles of the lowest frequency is considered as shown in Fig. 10.

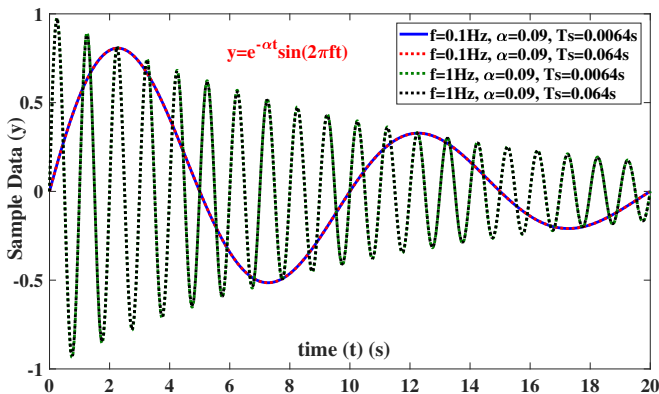


Fig. 10: Data requirement

4.2 MIMO Identification two-area system

To validate the effectiveness of the proposed MIMO identification algorithm in estimating the inter-area modes, a 3-ph fault is created on Bus-8 at 4s for a duration of 0.05s. The speed deviation after the fault is shown in Fig. 11. From visual inspection, it can be seen that the approximate frequency of oscillation is 0.6494Hz. From fast fourier transform (FFT) algorithm on ΔP_1 data, it can be seen that the frequency is 0.64Hz as well (see Fig. 12). The estimated transfer function between ΔP_1 (Bus-7 to Bus-8 to Bus-9) and u_4 (Generator-4) is shown in (19). Using the transfer function, the frequency obtained from the proposed algorithm considering mutual coupling is 0.6362Hz. Table 2 shows the inter-area mode comparison.

$$\begin{aligned}
 G_{14}(z) &= \frac{\Delta P_1(z)}{u_4(z)} \\
 &= \frac{59.2665 - 6.7181i}{1 - (0.9835 + 0.1257i)z^{-1}} \\
 &+ \frac{59.2665 + 6.7181i}{1 - (0.9835 - 0.1257i)z^{-1}} \\
 &+ \frac{-0.2852 + 38.1373i}{1 - (0.9300 + 0.2484i)z^{-1}} \\
 &+ \frac{-0.2852 - 38.1373i}{1 - (0.9300 - 0.2484i)z^{-1}} \\
 &+ \frac{-89.7368}{1 - 0.9961z^{-1}} - 28.9939
 \end{aligned} \tag{17}$$

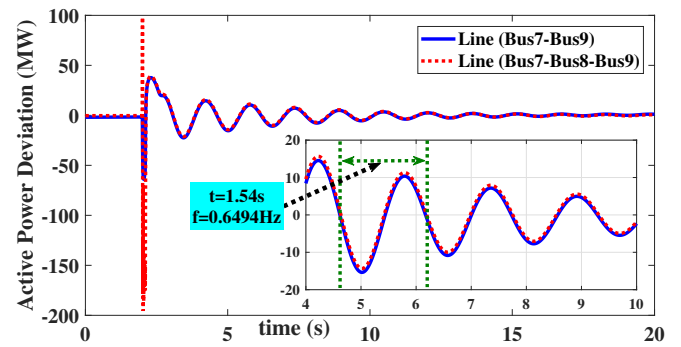


Fig. 11: Tie-lines active power deviation (ΔP_1)

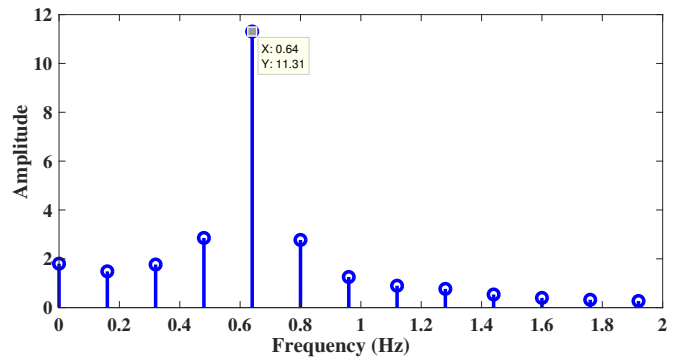


Fig. 12: FFT analysis of ΔP_1

Table 2 Inter-area mode comparison

Test System	MIMO Identification	FFT
Two Area	0.6362Hz	0.64Hz
IEEE 39-BUS	Case-1: 0.6077Hz Case-2: 0.6098Hz	Case-1: 0.599Hz Case-2: 0.6024Hz

4.3 MIMO Identification of 39-bus system

In order to show the scalability and usefulness of the algorithm, case studies with multiple disturbance with multiple machines are evaluated using IEEE 39 bus system. Two sequential disturbance cases at different locations as shown in Fig. 13 are simulated.

4.3.1 Case:1: In this case a 3-ph fault is created at 14s for a duration of 0.1s on bus-14. From Table 2 it can be seen that, using the proposed method, estimated inter-area frequency is 0.6077Hz whereas from FFT analysis of ΔP_1 (Bus-39 to Bus-1) data the inter-area frequency obtained is 0.599Hz (Fig. 14).

4.3.2 Case:2: In this case a 3-ph fault is created at 39.5s for a duration of 0.1s on bus-19. From Table 2 it can be seen that from the proposed method the estimated inter-area frequency is 0.6098Hz whereas from FFT analysis of ΔP_1 (Bus-39 to Bus-1) the inter-area frequency obtained is 0.6024Hz (Fig. 15). This proves that the proposed architecture can accurately represents the oscillation frequency.

5 Optimal Wide Area Control Loop Selection

After estimating the inter-area mode the objective is to damp that oscillation using WADC. However, in the MIMO power system model there are different input/output control loop combinations, it is important to estimate the most optimal control loop with which we can damp inter-area oscillations. This can be achieved by analyzing residues of the identified MIMO transfer functions corresponding to inter-area modes of interest [21]. For this, (13) is converted to continuous time domain format and rewritten in partial fraction form as shown in (18).

$$\begin{aligned} \mathbf{G}_{mp}(s) &= \frac{\Delta\omega_m(s)}{u_p(s)} \\ &= \frac{r_{mp}(1)}{s-p_1} + \frac{r_{mp}(2)}{s-p_2} + \dots + \frac{r_{mp}(j)}{s-p_j} + k_{mp}(s) \end{aligned} \quad (18)$$

The transfer function between ΔP_1 (Bus-7 to Bus-8 to Bus-9) and u_4 (Generator-4) using the proposed algorithm in continuous domain can be represented as (19).

$$\begin{aligned} \mathbf{G}_{14}(z) &= \frac{\Delta P_1(s)}{u_4(s)} \\ &= \frac{-15.127 + 1211.8i}{s - (-1.2121 + 8.2017i)} \\ &+ \frac{-15.127 - 1211.8i}{s - (-1.2121 - 8.2017i)} \\ &+ \frac{1859.7 - 209.77i}{s - (-0.26881 + 3.9774i)} \\ &+ \frac{1859.7 + 209.77i}{s - (-0.26881 - 3.9774i)} \\ &+ \frac{-2804.3}{s - (-0.12207)} - 10.142 \end{aligned} \quad (19)$$

where p and r_{mp} are the poles and residues of the transfer function $G_{mp}(s)$. The residue ($r_{mp}(j)$) corresponding to inter-area mode (p_j) gives the information of the optimal control loop. For a mode

p_j , the value of residue gives how controllable is the output ΔP_m and how observable is the input u_p , meaning how strong is the control loop to damp oscillations. It can be concluded that the control loop which has larger residue is the optimal loop.

5.1 Identifying the optimal control loop for two-area system

From Table 2 it can be seen that the dominant inter-area mode for two-area power system model is 0.6362Hz. The residue analysis corresponding to the inter-area mode of frequency 0.6362Hz is shown in Table 3. From Table 3 it can be seen that the maximum value of residue is for $\Delta P_1 \rightarrow u_3$ loop which is the most optimal. From this, generator-3 is the most controllable and the active power deviation ΔP_1 is the most observable signal.

Table 3 Optimal wide area control loop based on normalized residue analysis

output/input	u_1	u_2	u_3	u_4
ΔP_1 (Bus-7 to Bus-8 to Bus-9)	0.3335	0.42875	1	0.44531
ΔP_2 (Bus-7 to Bus-9)	0.32973	0.42015	0.99597	0.47881

5.2 Identifying the optimal control loop for 39 bus system

For 39 bus system, different cases are analyzed as discussed in Section 4.3.1 and 4.3.2 to illustrate how changes in operating conditions affect the inter-area modes and corresponding optimal control loops.

5.2.1 Case: 1: From Table 2 dominant inter-area mode for 39 bus system, case-1 is 0.6077Hz. The residue analysis corresponding to inter-area mode of frequency 0.6077Hz for top three control loops are shown in Table 4. From Table 4 it can be seen that generator-1, generator-8, and generator-9 are the most controllable and the corresponding observable signals are ΔP_2 , ΔP_1 , and ΔP_2 respectively.

Table 4 Optimal control loop for IEEE 39-bus (Fault on Bus-14)

Control Loop	Residue
ΔP_2 (Bus-39 to Bus-9) to u_1	1.0
ΔP_1 (Bus-39 to Bus-1) to u_8	0.8051
ΔP_2 (Bus-39 to Bus-9) to u_9	0.7350

5.2.2 Case: 2: From Table 2 dominant inter-area mode for 39 bus system, case-2 is 0.6098Hz. The residue analysis corresponding to inter-area mode of frequency 0.6098Hz for top three control loops are shown in Table 5. From Table 5 it can be seen that generator-10, generator-1, and generator-8 are the most controllable and the corresponding observable signals are ΔP_5 , ΔP_5 , and ΔP_1 respectively.

Table 5 Optimal control loop for IEEE 39-bus (Fault on Bus-19)

Control Loop	Residue
ΔP_5 (Bus-16 to Bus-17) to u_{10}	1.0
ΔP_5 (Bus-16 to Bus-17) to u_1	0.6993
ΔP_1 (Bus-39 to Bus-1) to u_8	0.4738

6 Measurement based DLQR and Kalman filter design

The WADC design is based on DLQR and KF. The WADC design architecture is as shown in Fig. 16.

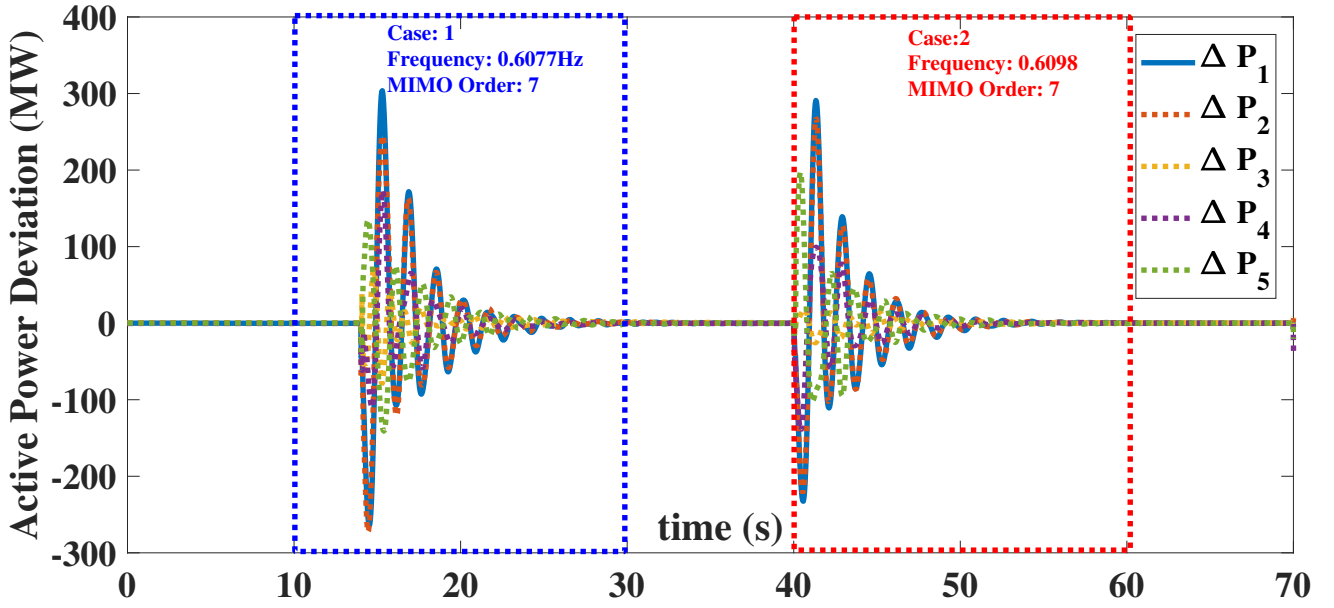


Fig. 13: 39 bus tie-line active power deviation

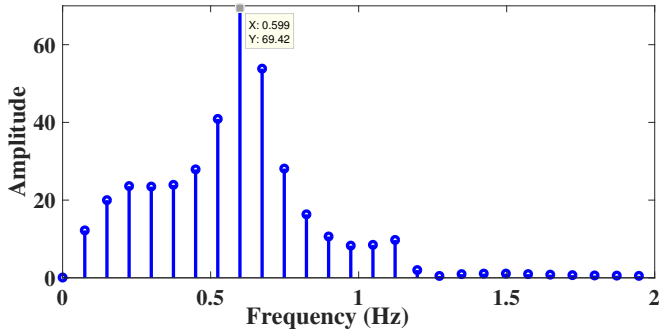


Fig. 14: FFT analysis of ΔP_1 (Case:1)

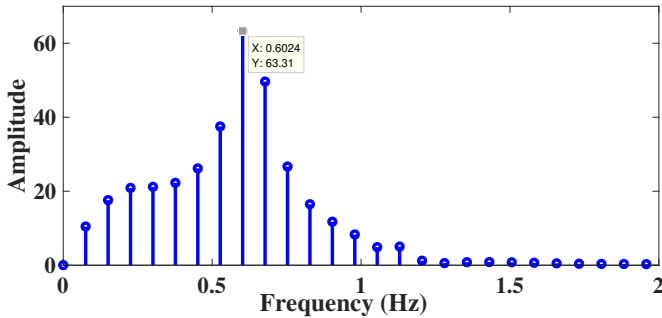


Fig. 15: FFT analysis of ΔP_1 (Case:2)

6.1 Discrete-time linear quadratic regulator

The DLQR based controller uses state space matrices corresponding to optimal control loop for calculating the control gain. For this the discrete state space model is extracted from the MIMO transfer functions (13) and represented as follows:

$$\begin{aligned} x_{k+1} &= A_k x_k + B_k u_k \\ y_k &= C_k x_k + D_k u_k \end{aligned} \quad (20)$$

where A , B , C , and D are the state, input, output, and feed forward matrices respectively. The objective of the DLQR is to minimize

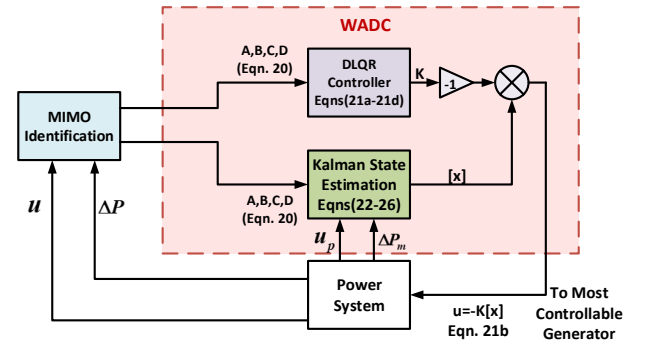


Fig. 16: WADC architecture

the cost of the objective function represented as (21a), where $R = \rho I$ ($\rho > 0$), $Q = C_k^T C_k$ are the weight matrices and N is the number of samples. The cost function can be minimized by calculating optimal control gain K by solving (21c)-(21d). The P in (21c) is the solution of the discrete algebraic Ricatti equations represented as (21d). The optimal control signal is represented as (21b) [22] which is sent to most controllable generator estimated from residue analysis.

$$J = \sum_{k=0}^N (x_k^T Q x_k + u_k^T R u_k) \quad (21a)$$

$$u_k = -K_k x_k \quad (21b)$$

$$K_k = (R + B_k^T P_{k+1} B_k)^{-1} B_k^T P_{k+1} A_k \quad (21c)$$

$$\begin{aligned} P_{k-1} &= Q + A_k^T P_k A_k \\ &\quad - A_k^T P_k B_k (R + B_k^T P_k B_k)^{-1} B_k^T P_k A_k \end{aligned} \quad (21d)$$

Table 6 shows the estimated optimal control gains for two-area system. Table 7 and Table 8 shows the optimal control gains for 39-bus system Case 1 and 2 respectively.

Table 6 Estimated LQR gains (K) for two-area system

Control Loop	Gain (K)
ΔP_1 to u_3	[0.089446 -0.1349 0.073803 -0.033455 0.019523]

Table 7 Estimated LQR gains (K) for IEEE 39 bus system (Case:1)

Control Loop	Gain (K)
ΔP_2 to u_1	[0.0041 -0.0065 -0.0029 0.0295 -0.0407 0.0233 -0.0190]
ΔP_1 to u_8	[-0.0467 0.1225 -0.2635 0.2954 -0.1783 0.0519 -0.0188]
ΔP_2 to u_9	[-0.0296 0.0884 -0.2031 0.2372 -0.1477 0.0448 -0.0188]

Table 8 Estimated LQR gains (K) for IEEE 39 bus system (Case:2)

Control Loop	Gain (K)
ΔP_5 to u_{10}	[-0.0919 0.3275 -0.4145 0.2566 -0.1636 0.0933 -0.0207]
ΔP_5 to u_1	[-0.0858 0.3297 -0.4227 0.2606 -0.1645 0.0931 -0.0207]
ΔP_1 to u_8	[-0.0445 0.1546 -0.1984 0.1249 -0.0807 0.0465 -0.0104]

6.2 Kalman filtering based state estimation

The optimal control signal in (21b) is the product of the optimal control gain and states of the system corresponding to optimal control loop. Here, KF technique is adapted to estimate the states of the system. The state space model as shown in (20) is used to estimate the states. The predictor step and co-variance calculation is given by (22) and (23) respectively.

$$x_{k+1} = A_k x_k + B_k u_k \quad (22)$$

$$L_k = A_k L_{k-1} A_k^T + Q_k \quad (23)$$

where Q and L are co-variance of noise and state vector estimate respectively. The Kalman gain factor (G) is estimated as shown in (24)

$$G_k = L_k H_k^T (H_k L_k H_k^T + R_k)^{-1} \quad (24)$$

where R and H are co-variance of measurement noise and the observation matrix respectively. The corrector step is represented as shown in (25) and (26).

$$x_k = x_{k+1} + G_k (z - H_k x_k + 1) \quad (25)$$

$$L_k = L_{k+1} - K_k H_k L_{k+1} \quad (26)$$

Further details of kalman filtering based state estimation are reported in [23].

7 Simulation Results

The output of WADC is sent to the most controllable generator as shown in Fig. 16. Implementation results on two-area and IEEE 39 bus system models considering various disturbances are illustrated next.

7.1 Simulation results of two-area system

The wide area control loop for two-area system is as shown in Fig. 17. Fig. 18 shows the speed deviation of generator 2 with and without WADC. Fig. 19 shows the speed deviation of generator 4 with and without WADC. Fig. 20 shows the tie-line active power deviation ΔP_1 . Fig. 21 shows the WADC output sent to generator 3. From the above figures it can be seen that the with the proposed approach the

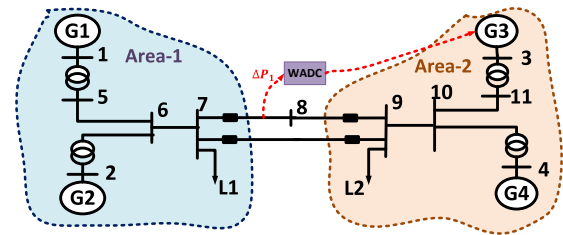
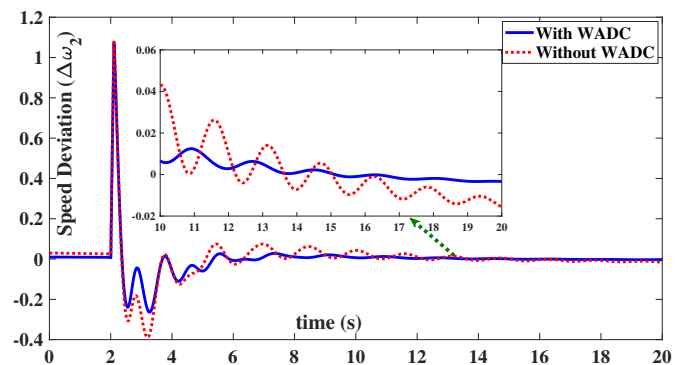
oscillations are damped effectively. Table 9 shows the comparison of performance metrics with and without WADC. The speed deviation value for generator-2 without WADC at 11s after disturbance is 0.01773 whereas with WADC the value is 0.0038. This indicates that there is 78.68% reduction in oscillation magnitude. In the same way for generator-4 there is 72.60% reduction in oscillation magnitude. Further area-under the curve for the absolute value of oscillations is analyzed as shown in Table 10 and found that for generator-2 the area under the curve is 66% less with WADC and for generator-4 it is 56% less. The area under the curve for tie-line power flow deviation is 51% less with WADC.

Table 9 Performance metrics for two-area system

Variable	Without WADC	With WADC
Peak $\Delta\omega_2$ at 15s (Fig. 18)	0.01773	0.0038
Peak $\Delta\omega_4$ at 14.25s (Fig. 20)	0.0413	0.0113

Table 10 Area under the curve for two-area system

Variable	Without WADC	With WADC
$\Delta\omega_2$ (Fig. 18)	0.4817	0.1638
$\Delta\omega_4$ (Fig. 19)	0.6959	0.3012
ΔP_1 (Fig. 20)	11.739	5.75

**Fig. 17:** Optimal control loop for two-area system**Fig. 18:** Generator-2 speed deviation (rad/s)

7.1.1 Effect of time-delay on two-area system control: To study the effect of time-delay on the control, an intentional time-delay is created in addition to the inherent time delay. The inherent time delay for the two-area system case is 0.15s. The intentional time delay is created in the control loop at the time delay block as shown in Fig. 1. Initially, a time delay of 1ms is created which is

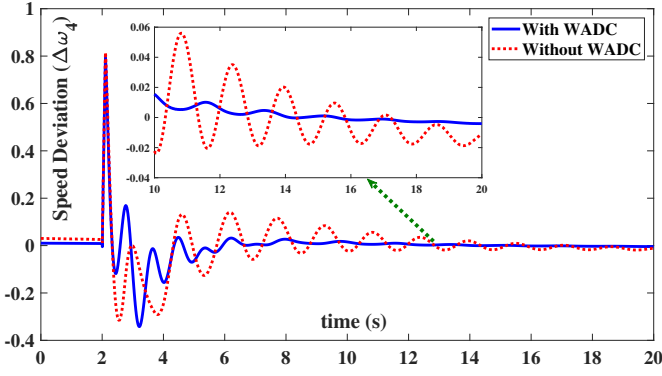


Fig. 19: Generator-4 speed deviation (rad/s)

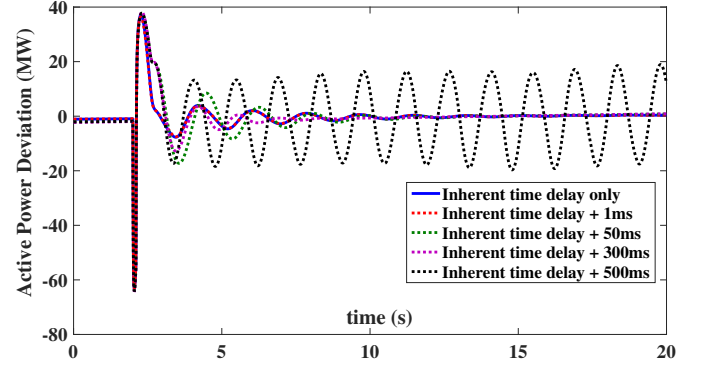


Fig. 22: Tie-line active power flow deviation (ΔP_1)

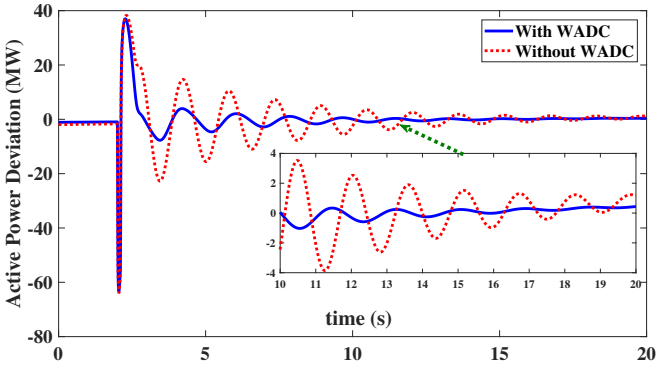


Fig. 20: Tie-line active power flow deviation (ΔP_1)

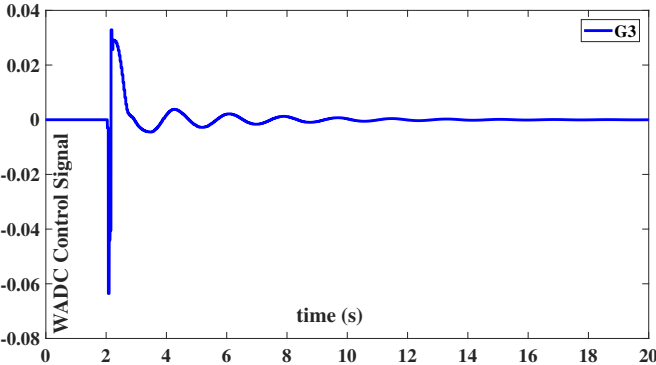


Fig. 21: WADC output signal

further increased up to 500ms. It can be observed from Fig. 22 that for an extra time delay of 500ms the controller performance started to deteriorate and as the time delay is increased further the system is driven into unstable mode. For quantitative analysis, relative error is calculated using (27).

$$relative\ error = \frac{\|\Delta P_{ref} - \Delta P_{delay}\|_2}{\|\Delta P_{ref}\|_2} \quad (27)$$

where ΔP_{ref} represents the response with inherent time delay and ΔP_{delay} represents the response with intentional time delay. Table 11 shows the relative error comparison for different time delays. It can be seen that the error increases as the time delay increases.

7.2 Simulation results of 39 bus system

For this system two cases are analyzed for different disturbances.

Table 11 Relative error for various time delays (two-area system)

Time Delay	Relative Error
1ms	0.029319
50ms	0.42091
300ms	0.52231
500ms	1.7834

7.2.1 *Case:1:* For the same disturbance scenario as discussed in Section 4.3.1, Fig. 23 and Fig. 24 shows the active power deviations ΔP_2 , and ΔP_4 respectively. Fig. 25, and Fig. 26 shows the speed deviations of generator 4, and 10 with and without WADC respectively. Fig. 27 shows the WADC output sent to most controllable generator. From the above figures it can be seen that with the proposed approach oscillations are damped effectively. The area under the curve for absolute value of speed deviations are analyzed as shown in Table 12 and it is found that the area under the curve is reduced by 59%, and 60.56% with WADC for generators 4, and 10 respectively.

Table 12 Area under the curve metric (39 bus system case:1)

Variable	Without WADC	With WADC
$\Delta\omega_4$ (Fig. 25)	6.3374	2.7498
$\Delta\omega_{10}$ (Fig. 26)	6.3081	2.4878

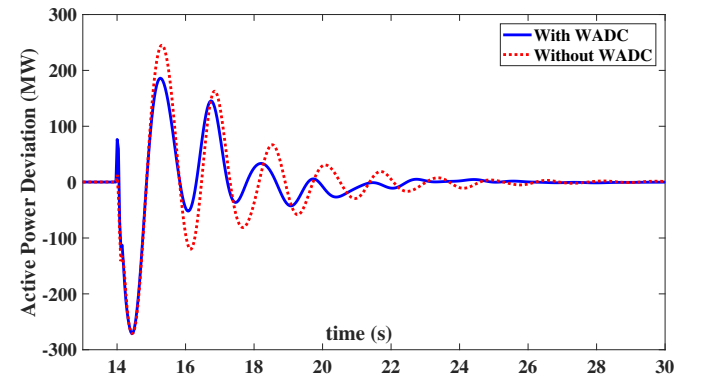


Fig. 23: Tie-line active power flow deviation (ΔP_2 (Bus-39 to Bus-9))

7.2.2 *Case:2:* For the same disturbance scenario as discussed in Section 4.3.2. Fig. 29 and Fig. 30 shows the active power deviations ΔP_2 , and ΔP_4 respectively. Fig. 31, and Fig. 32 shows the speed deviations of generator 7, and 10 with and without WADC respectively. Fig. 33 shows the WADC output sent to most controllable

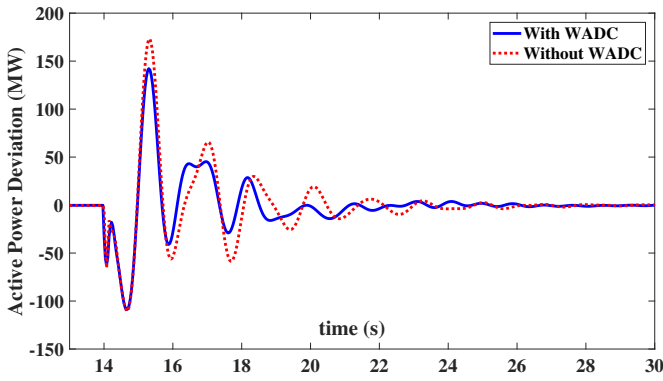


Fig. 24: Tie-line active power flow deviation (ΔP_4 (Bus-14 to Bus-15))

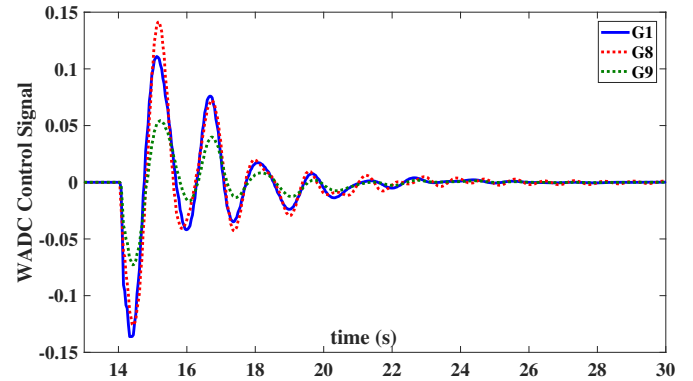


Fig. 27: WADC output signal

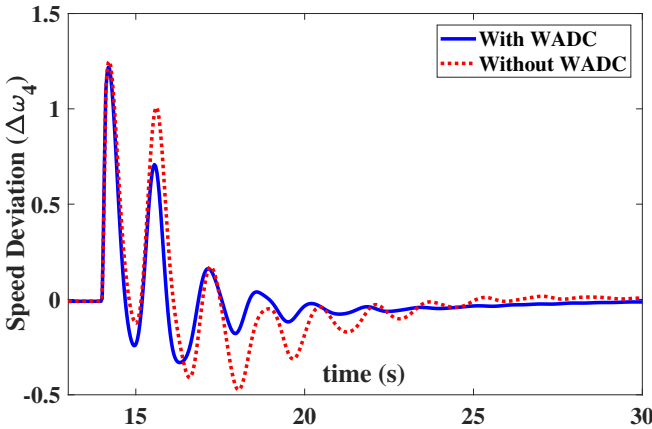


Fig. 25: Generator-4 speed deviation (rad/s)

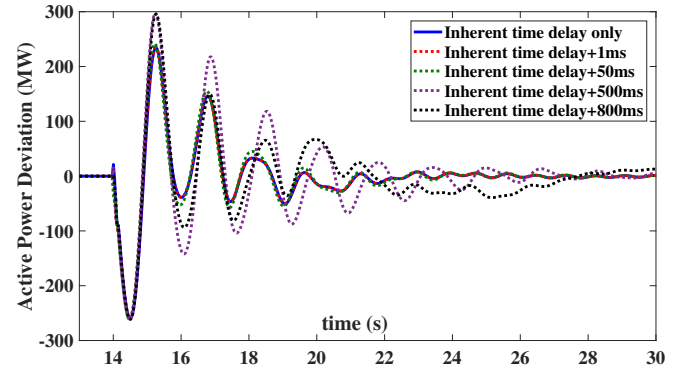


Fig. 28: Tie-line active power flow deviation (ΔP_1)

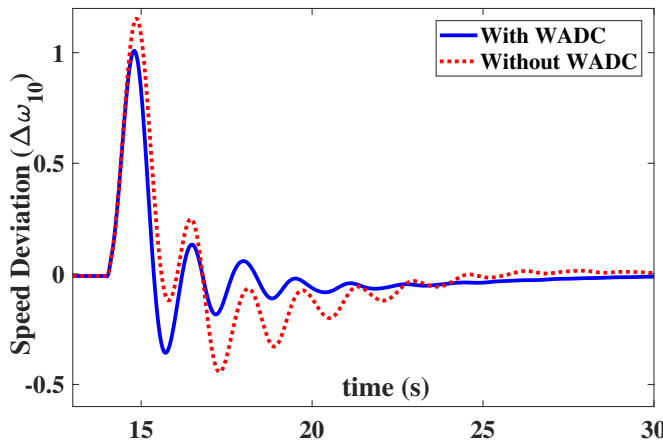


Fig. 26: Generator-10 speed deviation (rad/s)

Table 13 Area under the curve metric (39 bus system case:2)

Variable	Without WADC	With WADC
$\Delta\omega_7$ (Fig. 31)	3.746	1.7233
$\Delta\omega_{10}$ (Fig. 32)	3.5383	1.5359

generator. From the above mentioned figures it can be seen that the with the proposed approach the oscillations are damped effectively. The area under the curve for absolute value of speed deviations are analyzed as shown in Table 13 and it is found that the area under the curve is reduced by 54%, and 56% with WADC for generators 7, and 10 respectively.

7.2.3 Effect of time-delay on 39 bus system control: The inherent time delay for the 39 bus system case is 0.23s. The intentional time delay is created in the control loop at the time delay block as shown in Fig. 1. Initially, a time delay of 1ms is created and increased up to 800ms. It can be observed from Fig. 28 and

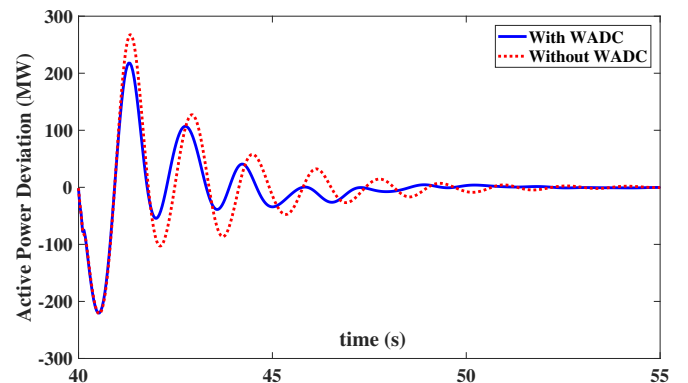


Fig. 29: Tie-line active power flow deviation (ΔP_2 (Bus-39 to Bus-9))

Fig. 34 that for an extra time delay of 500ms the controller performance started to deteriorate and as the time delay is increased further the system oscillations also increased. Table 14 shows the relative error comparison for 39 bus system for various time delays calculated using (27). In this case also the relative error increases as the time delay increases.

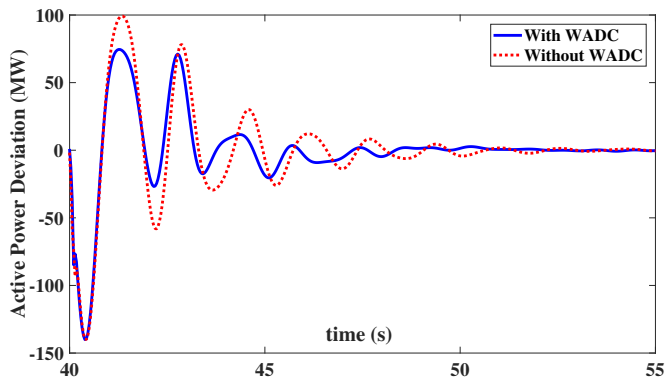


Fig. 30: Tie-line active power flow deviation (ΔP_4 (Bus-14 to Bus-15))

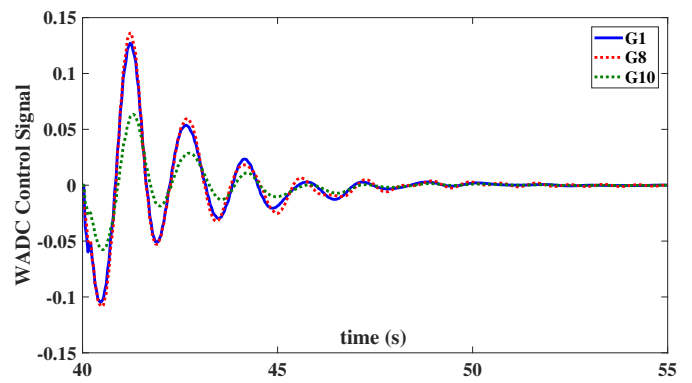


Fig. 33: WADC output signal

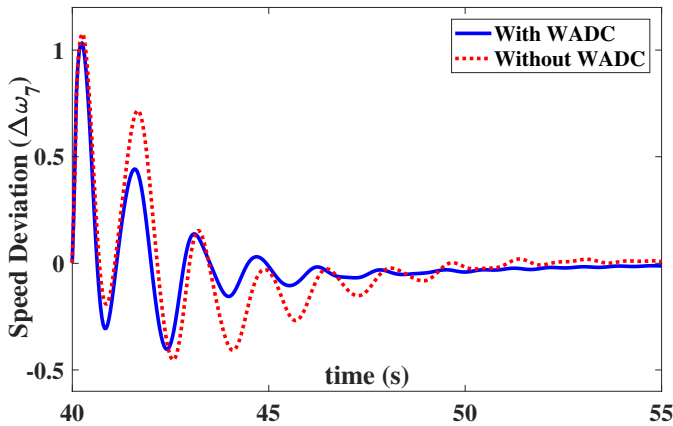


Fig. 31: Generator-7 speed deviation (rad/s)

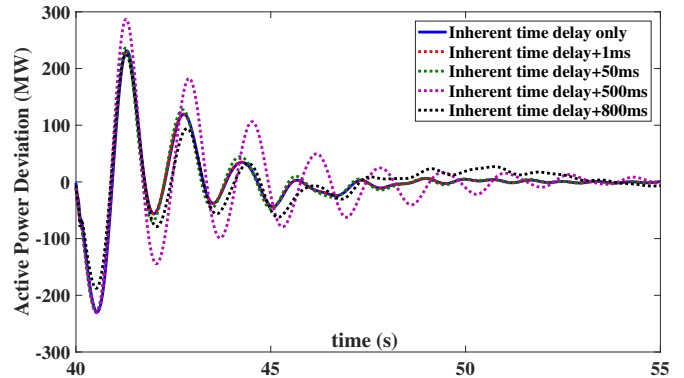


Fig. 34: Tie-line active power flow deviation (ΔP_1)

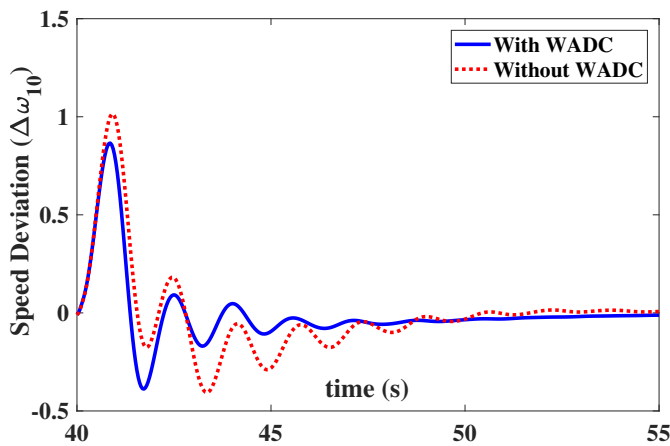


Fig. 32: Generator-10 speed deviation (rad/s)

8 Conclusion

The proposed method for measurement based wide area damping of inter-area oscillations based on MIMO identification overcome the drawbacks of earlier linearization based methods reported in literature. In this approach, initially MIMO system transfer functions are identified, then the inter-area modes are estimated using the MIMO transfer functions. The optimal control loop required for WADC is estimated through residues corresponding to the inter-area mode of interest. Finally, the WADC is design based on a combination of DLQR and Kalman filtering algorithms. The effectiveness of the proposed algorithm is verified by implementing on two-area and

Table 14 Relative error for various time delays (39 bus system)

	Case:1	Case:2
Time Delay	Relative Error	Relative Error
1ms	0.0526	0.0376
50ms	0.1469	0.1311
300ms	0.4979	0.3216
500ms	0.6429	0.6418

IEEE 39 bus power system models on RTDS/RSCAD and MATLAB based real-time co-simulation platform. In the future, framework to mitigate time-delay effects on the control action will be addressed.

9 References

- Klein, M., Rogers, G.J., Kundur, P.: 'A fundamental study of inter-area oscillations in power systems', *IEEE Transactions on Power Systems*, 1991, **6**, (3), pp. 914–921
- Chow, J.H.: 'Power System Coherency and Model Reduction'. Power Electronics and Power Systems. (Springer New York, 2014). Available from: <https://books.google.com/books?id=HGnABAAQBAJ>
- Rogers, G.: 'Power System Oscillations'. Power Electronics and Power Systems. (Springer US, 2012). Available from: <https://books.google.com/books?id=xOTTBwAAQBAJ>
- Yao, W., Jiang, L., Wen, J., Wu, Q.H., Cheng, S.: 'Wide-area damping controller of facts devices for inter-area oscillations considering communication time delays', *IEEE Transactions on Power Systems*, 2014, **29**, (1), pp. 318–329
- Azad, S.P., Irvani, R., Tate, J.E.: 'Damping inter-area oscillations based on a model predictive control (mpc) hvdc supplementary controller', *IEEE Transactions on Power Systems*, 2013, **28**, (3), pp. 3174–3183
- Pal, B., Chaudhuri, B.: 'Robust Control in Power Systems'. Power Electronics and Power Systems. (Springer US, 2006). Available from: <https://books.google.com/books?id=UXh1o196-McC>
- Juanjuan, W., Chuang, F., Yao, Z.: 'Design of WAMS-based multiple HVDC damping control system', *IEEE Trans Smart Grid*, 2008, **2**, pp. 572–581
- Li, Y., Rehtanz, C., Ruberg, S., Luo, L., Cao, Y.: 'Wide-area robust coordination approach of HVDC and FACTS controllers for damping multiple inter-area oscillations', *IEEE Trans Power Del*, 2012, **27**, pp. 1096–1105
- Kunjumammed, L.P., Singh, R., Pal, B.C.: 'Robust signal selection for damping of inter-area oscillations', *Proc IET Gener Transm Distrib*, 2012, **6**, pp. 404–416

- 10 Li, Y., Rehtanz, C., Ruberg, S., Luo, L., Cao, Y.: 'Assessment and choice of input signals for multiple HVDC and FACTS wide-area damping controllers', *IEEE Trans Power Syst.*, 2012, **27**, pp. 1969–1977
- 11 Dominguez.Garcia, J.L., Ugalde.Loo, C.E., Binachi, F., GomisBellmunt, O.: 'Input and output signal selection for damping of power system oscillations using wind power plants', *Int J Electr Power Energy Syst.*, 2014, **58**, pp. 75–84
- 12 Nguyen.Duc, H., Dessaint, L., Okou, A.F., Kamwa, I.: 'Selection of input/output signals for wide area control loops'. In: Proc. IEEE Power & Energy Society General Meeting. (, 2010. pp. 1–7
- 13 Zacharia, L., Hadjidemetriou, L., Kyriakides, E.: 'Integration of renewables into the wide area control scheme for damping power oscillations', *IEEE Trans Power Syst.*, 2018, **PP**, pp. 1–9
- 14 Pradhan, V., Kulkarni, A.M., Khaparde, S.A.: 'A model-free approach for emergency damping control using wide area measurements', *IEEE Trans Power Syst.*, 2018, **PP**, pp. 1–11
- 15 Musleh, A.S., Muyeen, S.M., AlDurra, A., Kamwa, I.: 'Testing and validation of wide-area control of statcom using real-time digital simulator with hybrid hilãÅsil configuration', *IET Gener Transm Distrib.*, 2017, **11**, pp. 3039–3049
- 16 Liu, H., Zhu, L., Pan, Z., Bai, F., Liu, Y., Liu, Y., et al.: 'Armax-based transfer function model identification using wide-area measurement for adaptive and coordinated damping control', *IEEE Transactions on Smart Grid.*, 2017, **8**, (3), pp. 1105–1115
- 17 B..B..Padhy, S.C.S., Verma, N.K.: 'A coherency-based approach for signal selection for wide area stabilizing control in power systems', *IEEE Systems Journal.*, 2013, **7**, (4), pp. 807–816
- 18 Sanchez.Gasca, J.J., Chow, J.H.: 'Performance comparison of three identification methods for the analysis of electromechanical oscillations', *IEEE Trans on Power Syst.*, 1999, **14**, (3), pp. 995–1002
- 19 'Control systems/mimo systems'. (, . Available from: https://en.wikibooks.org/wiki/Control_Systems/MIMO_Systems
- 20 'Gtnetx2: the powerful new network interface card'. (, . Available from: <https://www.rtds.com/gtnetx2-the-powerful-new-network-interface-card/>
- 21 Thakallapelli, A., Hossain, S.J., Kamalasadana, S.: 'Coherency based online wide area control of wind integrated power grid'. In: 2016 IEEE International Conference on Power Electronics, Drives and Energy Systems (PEDES). (, 2016. pp. 1–6
- 22 Zhang, W., Hu, J., Abate, A.: 'On the value functions of the discrete-time switched lqr problem', *IEEE Transactions on Automatic Control.*, 2009, **54**, (11), pp. 2669–2674
- 23 Zhang, J., Welch, G., Bishop, G., Huang, Z.: 'A two-stage kalman filter approach for robust and real-time power system state estimation', *IEEE Transactions on Sustainable Energy.*, 2014, **5**, (2), pp. 629–636